



Energy-efficient fabrication of a novel multivalence Mn_3O_4 - MnO_2 heterojunction for dye degradation under visible light irradiation

Jianhui Zhao ^a, Jun Nan ^{a,*}, Zhiwei Zhao ^{a,b,*}, Ning Li ^a, Jie Liu ^b, Fuyi Cui ^a

^a State Key Laboratory of Urban Water Resource and Environment, School of Municipal and Environmental Engineering, Harbin Institute of Technology, Harbin 150090, China

^b Department of National Defense Construction Planning and Environmental Engineering, Logistical Engineering University, Chongqing 401311, China



ARTICLE INFO

Article history:

Received 29 July 2016

Received in revised form

24 September 2016

Accepted 26 September 2016

Available online 28 September 2016

Keywords:

Valence state heterojunction

Mn_3O_4 - MnO_2 photocatalyst

Core-shell structure

Visible light driven

Dye degradation

ABSTRACT

A novel Mn_3O_4 - MnO_2 valence state heterojunction was fabricated for the first time by a low-temperature hydrothermal method and further applied for methylene blue (MB) degradation under visible light irradiation at room temperature. The Mn_3O_4 core with tetragonal hausmannite structure was coated by a thin amorphous MnO_2 shell. The specific surface area and light-response range of Mn_3O_4 - MnO_2 photocatalyst were significantly enhanced by doping MnO_2 . Noticeably, the Mn_3O_4 - MnO_2 exhibited excellent photocatalytic activity with the degradation efficiency of MB up to 93.5% within 1 h. Moreover, the mechanism for MB photocatalytic degradation by Mn_3O_4 - MnO_2 was also explored. The superoxide radicals made a major contribution to the photo-degradation process, followed by the photo-induced holes and hydroxyl radicals. The surface oxygen of Mn_3O_4 - MnO_2 also took part in the formation of superoxide radicals, which could be replenished by atmospheric oxygen. More importantly, the formation of type II heterojunction in Mn_3O_4 - MnO_2 composite could accelerate the spatial separation of photo-induced carriers. This novel multivalence Mn_3O_4 - MnO_2 core-shell composite photocatalyst proved to have great potentials for organic contaminants degradation in water.

© 2016 Elsevier B.V. All rights reserved.

1. Introduction

With the development of modern industry, organic compounds such as dyes, pesticides, pharmaceuticals and phthalate esters in environment, especially in water body, have been detected frequently [1–3]. Researches have reported that these organic compounds are posing serious threats to human health and environmental sustainability due to their toxicity and persistence, which has aroused great concern worldwide [4–6].

Conventional water treatment processes including biodegradation and adsorption can remove most organic compounds from wastewater. Nevertheless, the biodegradation process is relatively slow and ineffective for treatment of toxic organics due to the sensitivity of organisms [7]. Although these pollutants can be transferred from polluted water to solid by adsorption technology, they still need further treatment [8]. Alternatively, advanced oxidation technology can degrade refractory organic pollutants from water thoroughly, reducing the harm to the environment and human

body fundamentally [9]. Among them, photocatalytic oxidation technology is believed to be the most green and promising strategy for contaminants removal because of the solar energy utilization and no additional oxidants [10,11]. As is known that the catalyst properties such as light-harvesting efficiency, band gap structure and surface area play important roles in photocatalytic activity. Thus, designing and developing a novel photocatalyst with high-efficiency should be a key point to solve the problem of organic pollution in water.

Various types of photocatalysts have been fabricated ranging from one-component of titanium dioxide (TiO_2), zinc oxide (ZnO), stannic oxide (SnO_2), tungsten trioxide (WO_3) and graphite carbon nitride ($g-C_3N_4$) to multi-components of TiO_2 - and ZnO -based composites, silver- and bismuth-based compounds and so on [11–17]. As for the one-component photocatalysts, most of them had strong absorption in the ultraviolet range, while the absorption of visible light was low, being unable to make full use of the solar energy and declining their industrial values. Besides, the fast recombination of the photo-generated electrons and holes decreases their photocatalytic efficiency [18]. Although the multicomponent photocatalysts have enhanced the photocatalytic performance to some extent by extending the absorption region and prolonging the lifetime of carriers, the transfer process of photo carriers between

* Corresponding authors at: No.73, Huanghe Road, Nangang District, Harbin City, Heilongjiang Province, China.

E-mail addresses: hitnanjun@163.com (J. Nan), hit_zzw@163.com (Z. Zhao).

the bands of photocatalysts with different elements may cause energy loss, weakening their oxidation ability [18,19]. Recent studies have demonstrated that carriers and energy could be transferred facilely between different valence states of an element, which was beneficial to photocatalytic reactions [20–22]. As a green and bountiful resource, manganese with multivalence states (+2, +3, +4, +6 and +7) has attracted growing attentions in the photocatalytic field because they could be sensitized by visible light [22–24]. Lately, $\text{Mn}_3\text{O}_4/\text{MnCO}_3$ valence state heterojunction was successfully fabricated, which could degrade methylene blue (MB) and formaldehyde (CHOH) efficiently under synergistic effect of photo and thermal at high temperature (80°C) [22]. However, the broad band gap of Mn_3O_4 (2.3 eV) and MnCO_3 (5.0 eV) made them not fully utilize the whole visible light. More importantly, the whole process seemed to be energy-consumed because large amount of heat energy was needed not only in the preparation process but also in the reaction process.

Manganese dioxide (MnO_2), with a narrow bandgap and high surface area, could increase the utilization rate of visible light, which have significantly improved the photocatalytic performance of TiO_2 [25], bismuth oxyiodide (BiOI) [26] and mesoporous silica [27] under visible light irradiation. Manganous manganic oxide (Mn_3O_4) as a low-cost p-type semiconductor was also applied to promote the photocatalytic performance of composite photocatalysts [24]. The combination of Mn_3O_4 and MnO_2 would provide valuable advantages such as strong visible light absorption, more active sites and enhanced charge separation performance. Herein, the mixed-valent $\text{Mn}_3\text{O}_4\text{-MnO}_2$ heterojunction was fabricated for the first time by a facile and energy-effective method through a hydrothermal process at 363 K. The inexpensive MnCl_2 and KMnO_4 were applied as precursors of manganese element and no additional oxidizer or reductant was added in the synthetic process. The visible light absorption of $\text{Mn}_3\text{O}_4\text{-MnO}_2$ was dramatically enhanced, achieving highly MB degradation in visible light. The recombination of photo-carries was limited effectively by the formation of $\text{Mn}_3\text{O}_4\text{-MnO}_2$ heterojunction. Moreover, the major active species in the photocatalytic process were also identified. This novel $\text{Mn}_3\text{O}_4\text{-MnO}_2$ core-shell composite would enjoy bright prospect in photo-degradation of organic pollutants in water.

2. Experimental

2.1. Chemicals

All chemicals used in this study were analytical grade. Besides, deionized (DI) water was applied as solvent. Manganese chloride ($\text{MnCl}_2\cdot 4\text{H}_2\text{O}$), potassium permanganate (KMnO_4) and sodium hydroxide (NaOH) were supplied by Xilong Chemical Co., Ltd (Shantou, China) while Poly (vinylpyrrolidone) (PVP, K-30) was purchased from Sinopharm Chemical Reagent Co., Ltd (Shanghai, China).

2.2. Synthesis

The photocatalysts were fabricated with a low-temperature hydrothermal method at 363 K under continuous stirring. The specific operations were as follows.

2.2.1. Synthesis of Mn_3O_4 nanoparticles

The DI water (80 mL) in a glass bottle was heated to 363 K. Then 20 mL solution containing 4.5 mmol $\text{MnCl}_2\cdot 4\text{H}_2\text{O}$ and 1.0 g PVP was added to the glass bottle. After that, 4.5 mL NaOH (2.0 M) was immediately added to the mixture, producing light brown precipitate. The precipitate was aged in mother solution for 3 h under stirring. After the solution cooled to room temperature, the solid powder was separated by centrifugation and was washed three times with

DI water and ethanol, respectively. Finally, it was dried at 353 K in a vacuum drying oven.

2.2.2. Synthesis of $\text{Mn}_3\text{O}_4\text{-MnO}_2$ nanosheets

The $\text{Mn}_3\text{O}_4\text{-MnO}_2$ composite with molar ratio of $\text{Mn}_3\text{O}_4:\text{MnO}_2 = 2:5$ was fabricated. The DI water (80 mL) in a glass bottle was heated to 363 K. Then 20 mL solution containing 4.5 mmol $\text{MnCl}_2\cdot 4\text{H}_2\text{O}$ and 1.0 g PVP was added to the glass bottle. After that, 4.5 mL NaOH (2.0 M) was immediately added to the bottle, producing light brown precipitate. About 2 min later, 5.0 mL of 0.2 M KMnO_4 solution was added into the mixture and kept stirring for 3 h. The separation, washing and drying operations for $\text{Mn}_3\text{O}_4\text{-MnO}_2$ composite were the same as those for Mn_3O_4 nanoparticles. The $\text{Mn}_3\text{O}_4\text{-MnO}_2$ composites with molar ratios of 3:5 and 1:5 were also fabricated by adjusting the molar ratios of MnCl_2 and KMnO_4 . The samples were characterized by X-ray diffraction (XRD, Fig. S1), shown in the Supporting information. The composite $\text{Mn}_3\text{O}_4\text{-MnO}_2$ with ratio of $\text{Mn}_3\text{O}_4:\text{MnO}_2 = 2:5$ exhibited excellent photocatalytic activity (presented in Fig. S2), which was mainly investigated and reported in this paper.

2.2.3. Synthesis of MnO_2 nanoplates

The 4.5 mmol $\text{MnCl}_2\cdot 4\text{H}_2\text{O}$ and 1.0 g PVP were dissolved in 20 mL DI water. Then the solution was added to 80 mL DI water in a glass bottle which had been heated to 363 K using the heating stirrer. After that, 4.5 mL NaOH (2.0 M) was added to the glass bottle immediately. About 2 min later, 9.0 mL of 0.2 M KMnO_4 solution was added into the mixture and kept stirring for 3 h. The separation, washing and drying operations for MnO_2 nanoplates were the same as those for Mn_3O_4 nanoparticles.

2.3. Characterization

XRD patterns of the prepared samples were obtained using a diffractometer (Empyrean, Panalytical, Netherlands) equipped with $\text{Cu K}\alpha$ radiation. The chemical species of the samples were analyzed by X-ray photoelectron spectroscopy (XPS; Escalab 250Xi, Thermo Fisher Scientific, US) and all binding energies of the elements were calibrated referring to the C1s peak at 284.8 eV of adventitious carbon. Surface morphology of the samples was examined by a field-emission scanning electron microscopy (FESEM, HELIOS NanoLab 600i, US) after spraying a thin gold layer. Transmission electron microscopy (TEM) images, high-resolution transmission electron microscopy (HRTEM) images, selected-area electron diffraction (SAED) patterns and electron energy loss (EEL) spectra of the samples were acquired by a field-emission transmission electron microscopy (FETEM, Tecnai G2 F30, US) with an electron energy loss spectroscopy (ELLS) analyzer. The samples were also examined by Fourier transform infrared spectrometer (FTIR, Perkin Elmer, US) with scan range from 400 to 4000 cm^{-1} after pressing into tablets with KBr powder. The specific surface area of the samples were determined by the Brunauer-Emmett-Teller (BET) method at 77 K with an ASAP 2020 system (Quantachrome, US). Ultraviolet-visible (UV-vis) diffuse reflectance spectra was measured by the spectrophotometer (UV 2550, Shimadzu, Japan) with BaSO_4 as reference. The transient photocurrent response and electrochemical impedance spectroscopy (EIS) of the samples were measured in a three-electrode quartz cell in 0.1 M Na_2SO_4 electrolyte by an electrochemical work station (CHI-660B, China). The platinum (Pt) electrode and calomel electrode were worked as counter and reference electrodes, respectively. The indium-tin oxide (ITO) electrode coated with photocatalyst was used as the working electrode. The visible light was applied by a 300 W Xe lamp.

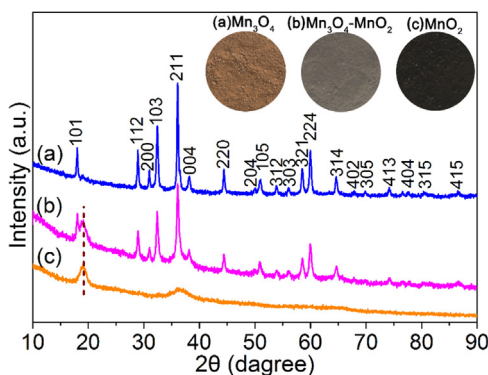


Fig. 1. XRD patterns of (a) Mn₃O₄, (b) Mn₃O₄-MnO₂ and (c) MnO₂. The insets were photographic images of Mn₃O₄, Mn₃O₄-MnO₂ and MnO₂ powders.

2.4. Photocatalytic reaction

The photocatalytic reactions were carried out in a 200 mL quartz beaker with 100 mL methylene blue (MB) solution at room temperature. The initial MB concentration was 10 mg/L and the catalyst dosage was determined as 0.5 g/L (Fig. S3). In the first 30 min, the suspensions were kept stirring in dark to reach adsorption-desorption equilibrium (Fig. S4). Then the MB solutions were degraded under visible light ($\lambda > 420$ nm) provided by a 300 W Xe lamp (NBET Technology Co., Ltd, China) equipped with two cutoff filters (UVCUT 400 and VisREF 780). The distance between the light source and the samples was 10 cm. At given time intervals, about 3.0 mL MB suspension was withdrawn by a pipette. After centrifuge-

gation, the solution concentrations were measured at 664 nm by an UV-vis spectrophotometer (T9, Persee, China). The reusability of the newly-fabricated composite catalyst was investigated by recycling the photo-degradation of MB. The separated photocatalyst was irradiated under visible light for 30 min to remove the adsorbed MB before the next photo-degradation experiment. Besides, the residual concentration of manganese in solution was measured by an inductively coupled plasma optical emission spectrometer (ICP-OES, Perkin Elmer Optima, US).

3. Results and discussion

3.1. Phase constitution and morphology of photocatalysts

The structures of the three as-prepared products were examined by X-ray diffraction (XRD) technique and the results were shown in Fig. 1. All the diffraction peaks in Fig. 1(a) were perfectly indexed to Mn₃O₄ with tetragonal hausmannite structure (space group: I4₁/amd, $a = 5.763 \text{ \AA}$, $c = 9.471 \text{ \AA}$, JCPDS NO. 24-0734) and no any other crystalline peaks was detected. Similarly, the diffraction peaks of tetragonal Mn₃O₄ were also observed in Fig. 1(b). Besides, a broad peak located at 20°–19.2° appeared, which was identified as amorphous MnO₂ [28]. The composite photocatalyst fabricated in this study was constituted of crystalline Mn₃O₄ and amorphous MnO₂. As shown in Fig. 1(c), two broad peaks at 19.2° and 37.0° were observed clearly, which were indexed to α -MnO₂ (JCPDS No. 44-0141) with amorphous state [29]. In the insets, the color of the fabricated Mn₃O₄, Mn₃O₄-MnO₂ and MnO₂ powders were brown, dark brown and black, respectively.

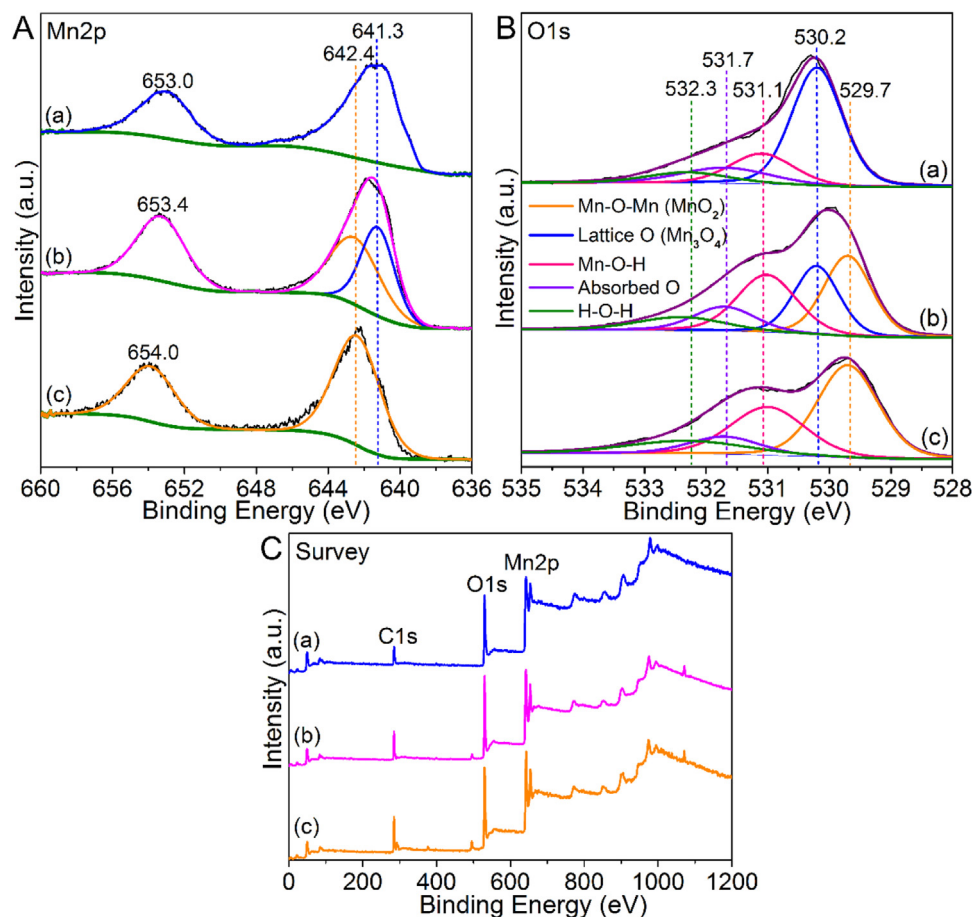


Fig. 2. The XPS spectra of (a) Mn₃O₄, (b) Mn₃O₄-MnO₂ and (c) MnO₂: (A) Mn 2p, (B) O 1s and (C) survey scan.

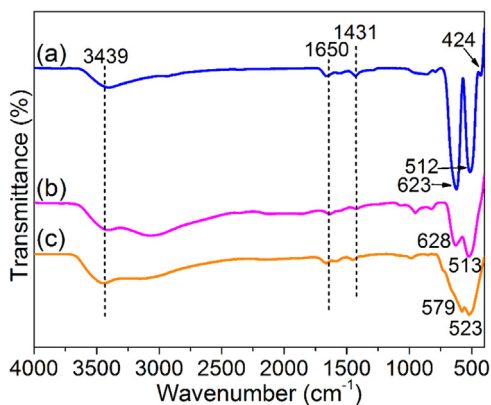


Fig. 3. FT-IR spectra of (a) Mn_3O_4 , (b) $\text{Mn}_3\text{O}_4\text{-MnO}_2$ and (c) MnO_2 .

To further determine the chemical composition of the photocatalysts, X-ray photoelectron spectroscopy (XPS) measurement was carried out. The XPS survey scan of the three photocatalysts were supplied in Fig. 2C, which showed the characteristic peaks of manganese (Mn), oxygen (O) and adventitious carbon (C). The high-resolution Mn 2p and O 1s spectra were presented in Fig. 2A and B, respectively. As shown in Fig. 2A, the peaks of Mn 2p_{3/2} were located at binding energy (BE) of 641.3 and 642.4 eV, which were consistent with the reported values of Mn_3O_4 and MnO_2 [28,30]. Thus the catalysts shown in Fig. 2A (a) and (c) were confirmed as pure Mn_3O_4 and MnO_2 . The Mn2p_{3/2} spectrum in Fig. 2A (b) demonstrated that the composite catalyst was composed of Mn_3O_4 and MnO_2 , including multivalent state manganese (Mn^{2+} , Mn^{3+} and Mn^{4+}). It was also obtained from XPS analysis that the Mn content in Mn_3O_4 and MnO_2 for the composite were 54.23% and 45.77% respectively, indicating the ratio of Mn_3O_4 and MnO_2 in the composite was about 2:5. Such a conclusion was further validated by the XPS results of O 1s. As shown in Fig. 2B, the BE values of approximately 529.7, 530.2, 531.1, 531.7 and 532.3 eV were corresponded to the bulk oxygen of MnO_2 , lattice oxygen of Mn_3O_4 , surface hydroxyl bonded to Mn, absorbed oxygen and adsorbed molecular water, respectively [22,30,31]. The corresponding oxygen species in $\text{Mn}_3\text{O}_4\text{-MnO}_2$ composite (Fig. 2B (b)) accounted for 29.62%, 23.71%, 26.18%, 11.53% and 8.96%, respectively. It was further confirmed that the ratio of Mn_3O_4 and MnO_2 in the composite was 2:5. Besides, it should be noted that the $\text{Mn}_3\text{O}_4\text{-MnO}_2$ composite possessed abundant surface oxygen, which played important roles in photocatalytic reactions [32].

Fourier transformation infrared spectroscopy (FTIR) measurements were performed to further identify the chemical bonds and functional groups in the photocatalysts. The infrared spectra were recorded and presented in Fig. 3. Among these absorption bands, the band around 3439 cm^{-1} was typically ascribed to the O–H stretching vibration of absorbed water molecules, and the other two bands located at 1650 and 1431 cm^{-1} were attributed to the bending vibration of hydroxyl combined with Mn atoms [31,33]. Besides, three characteristic absorption bands of Mn_3O_4 were observed in Fig. 3(a) with the range of $650\text{--}400\text{ cm}^{-1}$ [30]. The two broad bands at 623 and 512 cm^{-1} were correspond to the Mn–O stretching vibration in tetrahedral sites and distortion vibration in an octahedral environment, respectively. The band at 424 cm^{-1} was attributed to the stretching vibration of Mn^{3+} in the octahedral sites. As for the spectrum of MnO_2 in Fig. 3(c), two significant bands at 579 and 523 cm^{-1} were observed, which were associated with the Mn–O vibrations of MnO_6 octahedral framework in the MnO_2 [33]. Furthermore, the two asymmetric vibrations at 528 and 513 cm^{-1} for $\text{Mn}_3\text{O}_4\text{-MnO}_2$ composite in Fig. 3(b) should be

attributed to the vibration superposition of Mn–O in Mn_3O_4 and MnO_2 .

The typical scanning electron microscopy (SEM) and transmission electron microscopy (TEM) images of Mn_3O_4 , $\text{Mn}_3\text{O}_4\text{-MnO}_2$ and MnO_2 photocatalysts were shown in Fig. 4. As can be seen from Fig. 4(a–b), the morphology of pure Mn_3O_4 presented spherical particles with diameters ranging from 60 to 90 nm and the aggregation phenomena between Mn_3O_4 nanoparticles was observed. The lattice fringe of 0.493 nm could be clearly seen from the high resolution transmission electron microscopy (HRTEM) image in Fig. 4(c), corresponding to the (101) plane of Mn_3O_4 . The SEM image in Fig. 4(d) revealed that the $\text{Mn}_3\text{O}_4\text{-MnO}_2$ composite exhibited sheet structure with thickness of 20 nm approximately. From the TEM image in Fig. 4(e), it could be inferred that the $\text{Mn}_3\text{O}_4\text{-MnO}_2$ composite had core-shell structure, which was further identified by the HRTEM image enlarged from the TEM image. As shown in Fig. 4(f), the lattice fringes of 0.309 and 0.249 nm were assigned to the (112) and (211) crystal planes of Mn_3O_4 , respectively. Furthermore, the amorphous MnO_2 at the edge adhered on the Mn_3O_4 surface, indicating the core-shell structure of the $\text{Mn}_3\text{O}_4\text{-MnO}_2$ nanosheets. Besides, the core-shell structure was further confirmed by electron energy loss spectroscopy (EELS) analysis (Fig. S5, details were shown in Supporting information). The selected-area electron diffraction (SAED) pattern of $\text{Mn}_3\text{O}_4\text{-MnO}_2$ nanosheets was presented in the inset. The polycrystalline diffraction rings were corresponded to the (101), (112), (103), (211), (220), (105) and (321) planes of tetragonal hausmannite Mn_3O_4 . The crystal structure of $\text{Mn}_3\text{O}_4\text{-MnO}_2$ given by the SAED pattern and HRTEM image was consistent with the results obtained by XRD analysis. As shown in Fig. 4(g–i), the pure MnO_2 presented plate-like morphology and no obvious crystal lattice fringe could be observed form the HRTEM image, revealing its amorphous form.

3.2. The formation mechanism of photocatalysts

The formation mechanism of Mn_3O_4 nanoparticles, $\text{Mn}_3\text{O}_4\text{-MnO}_2$ core-shell nanosheets and MnO_2 nanoplates were proposed based on their composition and stoichiometric relationship. The fabrication processes were illustrated in Fig. 5. The growth mode and ultimate shape of the photocatalysts were directed by Poly (vinyl pyrrolidone) (PVP) [34]. The three photocatalysts shared the same reactions (Eqs. (1) and (2)) during the early prepared stage. When the 9.0 mmol NaOH was added to the mixture containing 4.5 mmol $\text{MnCl}_2\text{-}4\text{H}_2\text{O}$ and 1.0 g PVP, the white Mn(OH)_2 precipitate was produced by the reaction between MnCl_2 and NaOH under stirring. And then a fraction of Mn(OH)_2 was converted into brown MnO(OH)_2 under the influence of dissolved oxygen in water [35].



The Mn_3O_4 nanoparticles were fabricated without dosage of KMnO_4 into the system. It was suggested that the redox and dehydration reaction between Mn(OH)_2 and MnO(OH)_2 occurred (Eq. (3)). Besides, a part of Mn(OH)_2 precipitate might react with the dissolved oxygen directly (Eq. (4)). Also, the two reaction equations of Eqs. (2) and (3) can be combined into one equation written as Eq. (4). As is well known, the surface of larger nanoparticles with lower energy was more stable than that of small nanoparticles. The produced seed nucleus of small Mn_3O_4 nanoparticles were inclined to growth due to their high surface energy and ferromagnetism [36]. Meanwhile, PVP adsorbed on the surface of Mn_3O_4 nanoparticles to restrict their further growth. With the reaction continuing, the small Mn_3O_4 nanoparticles were gradually dissolved and contributed to the growth of large nanoparticles. The growth process would be continue until all the small Mn_3O_4 nanoparticles were

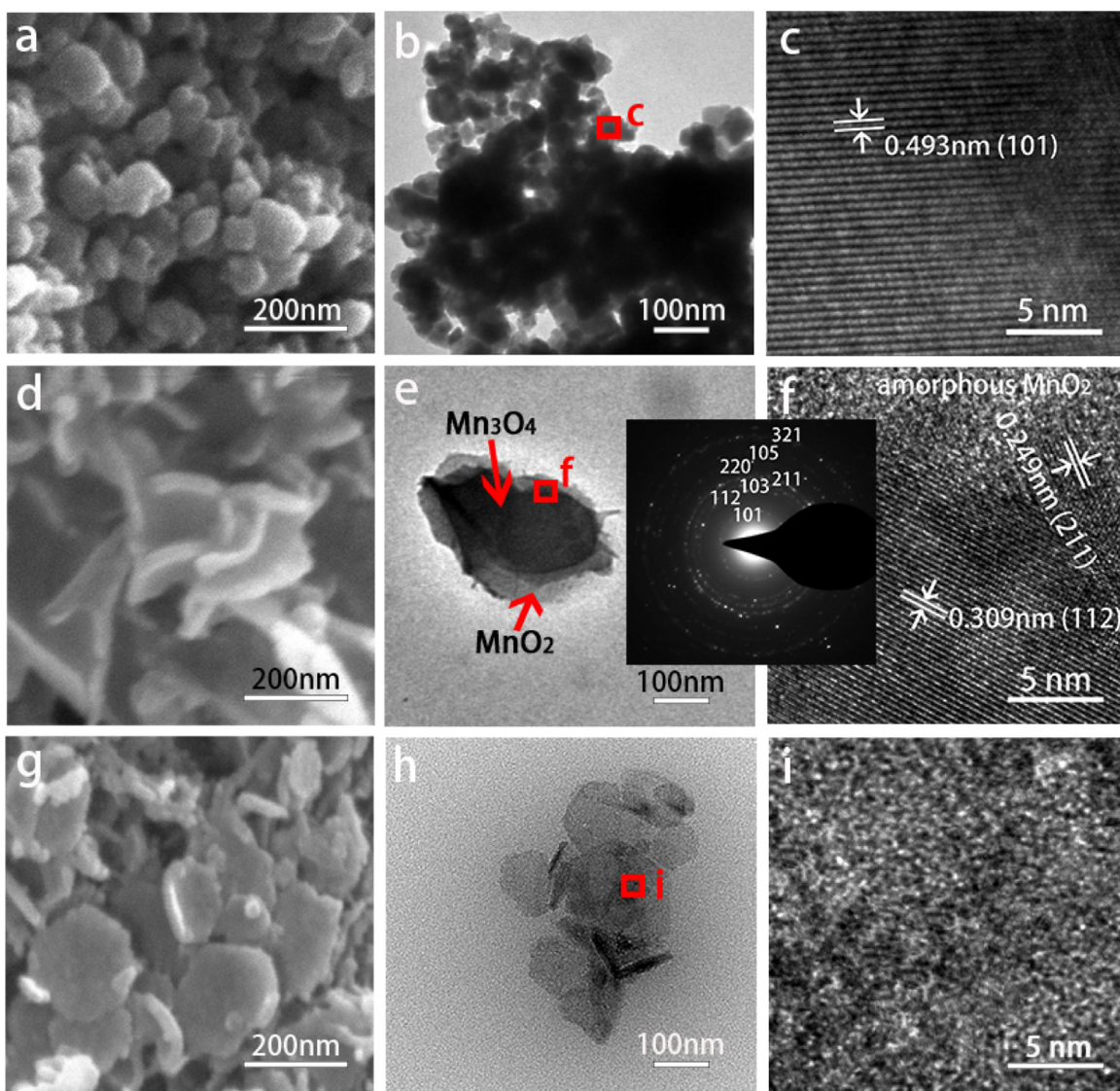


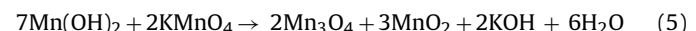
Fig. 4. SEM, TEM and HRTEM images of Mn₃O₄ (a–c), Mn₃O₄-MnO₂ (d–f) and MnO₂ (g–i). The inset between (e) and (f) displayed the SAED pattern of Mn₃O₄-MnO₂.

consumed completely, which was known as Ostwald ripening [34]. Finally, the Mn₃O₄ nanoparticles with relatively uniform size were fabricated by an isotropic growth mode.



In order to fabricate the Mn₃O₄-MnO₂ core-shell photocatalyst, 1.0 mmol KMnO₄ was added to the reaction system, then the redox reaction between Mn(OH)₂ and KMnO₄ took place rapidly with the precipitate color changing from light brown into dark brown (Eq. (5)). In addition, the MnO(OH)₂ precipitate was turned into MnO₂ by dehydration reaction (Eq. (6)). Similarly, the formed Mn₃O₄ acted as seed nucleus for the further growth of Mn₃O₄ nanoparticles. At the same time, the in situ generated MnO₂ could be adhered on the Mn₃O₄ surface by surface hydroxyl radicals, forming a thin shell. As the molar ratio of PVP to manganese source decreased, the coverage of PVP on the faces of the seeds was declined, then the growth mode of the small nanoparticles changed from isotropic growth to anisotropic growth. Generally, the formation of 2-dimensional (2D) structured nanomaterials is attributed to the anisotropic growth along a plane. In this case, one plane of nanoparticles was attached with PVP and the corresponding surface

energy decreased. Then the other plane of the nanoparticles with high surface energy was linked by adjacent nanoparticles. In brief, the relatively lower coverage of PVP on nanoparticles kept them growing along one plane, forming the 2D structured Mn₃O₄-MnO₂ core-shell nanosheets through Ostwald ripening.



The reaction process and ultimate products in our reaction system were obviously influenced by the variation of redox conditions. As presented in Eq. (7), with the dosage of KMnO₄ increasing to 1.8 mmol, the MnO₂ precipitate was produced immediately through the redox reaction between Mn(OH)₂ and KMnO₄. Besides, the MnO(OH)₂ precipitate was also converted into MnO₂ by dehydration reaction (Eq. (6)). The formation mechanism of 2D MnO₂ nanoplates was similar to that of Mn₃O₄-MnO₂ nanosheets. On this occasion, the generated MnO₂ nanoparticles also showed anisotropic growth mode at the surface covered by PVP incompletely. These small MnO₂ nanoparticles were bridged together

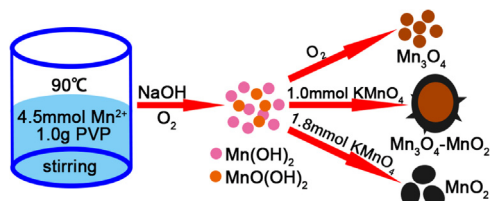
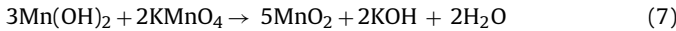


Fig. 5. Schematic illustration of the fabrication processes of Mn_3O_4 , $\text{Mn}_3\text{O}_4\text{-MnO}_2$ and MnO_2 .

along one plane through surface hydroxyl radicals, forming the 2D structured nanoplates by Ostwald ripening process.



3.3. Photocatalytic activities

To evaluate the photocatalytic activity of Mn_3O_4 nanoparticles, $\text{Mn}_3\text{O}_4\text{-MnO}_2$ nanosheets and MnO_2 nanoplates under visible light irradiation, the degradation of a model organic dye methylene blue (MB), was served for a probe reaction. As contrast, the experiments of MB degradation without photocatalysts in dark as well as under visible light irradiation were carried out. Besides, the MB removal with catalysts was mainly through simultaneous adsorption and degradation under illumination. Hence the adsorption experiments were also conducted in order to better study the photocatalytic performance of the photocatalysts. Before irradiation, The MB solution mixed with the catalysts were stirred for 30 min in dark to reach the absorption equilibrium. As can be seen from Fig. 6(a), the $\text{Mn}_3\text{O}_4\text{-MnO}_2$ core-shell composite exhibited the highest catalytic activity under visible light irradiation, which significantly outperformed the pure Mn_3O_4 and MnO_2 catalysts. The adsorption efficiency of Mn_3O_4 , $\text{Mn}_3\text{O}_4\text{-MnO}_2$ and MnO_2 were 11.1%, 31.0% and 36.5%, respectively. The higher adsorption capacity of $\text{Mn}_3\text{O}_4\text{-MnO}_2$ and MnO_2 might attribute to their higher surface area and more adsorp-

tion sites. In the contrast experiments, no MB was degraded in dark and 6.4% of MB was self-degraded under visible light irradiation for 1 h. After 1 h of visible light irradiation, 33.4%, 93.5% and 51.1% of MB dye could be degraded by Mn_3O_4 , $\text{Mn}_3\text{O}_4\text{-MnO}_2$ and MnO_2 photocatalysts, respectively. In order to further investigate the degradation kinetics, the first-order kinetic model was applied to fit the degradation data and the fitting results were shown in Fig. 6(b). It was apparent that all experimental data followed the first-order kinetic model. The self-degradation rate constant of MB under visible light irradiation was 0.0011 min^{-1} , while the degradation rate constants of MB for Mn_3O_4 , $\text{Mn}_3\text{O}_4\text{-MnO}_2$ and MnO_2 photocatalysts were 0.0068 , 0.0456 and 0.0119 min^{-1} , respectively. Obviously, the $\text{Mn}_3\text{O}_4\text{-MnO}_2$ core-shell composite exhibited the excellent activity under visible light irradiation, which was superior to the reported $\text{MnO}_2/\text{TiO}_2$ and $\text{Al}_2\text{O}_3\text{-Mn}_3\text{O}_4$ photocatalysts [25,37].

In general, the recyclability and stability are essential for the industrial applications of the photocatalysts. The MB degradation by $\text{Mn}_3\text{O}_4\text{-MnO}_2$ core-shell photocatalyst under visible light irradiation was carried out consecutively for five cycles. As shown in Fig. 6(c), the stable reusability of $\text{Mn}_3\text{O}_4\text{-MnO}_2$ was observed since the removal efficiency of MB only decreased by 6.0% after five cycles. Besides, the concentrations of manganese in the reaction solutions were below the detection limit ($0.5 \mu\text{g/L}$), indicating the stability of the $\text{Mn}_3\text{O}_4\text{-MnO}_2$ composite during the degradation process in aqueous solutions. The slight decrease of degradation efficiency with the increase in cycle might be resulted from the loss of $\text{Mn}_3\text{O}_4\text{-MnO}_2$ in the regeneration process. Therefore, the stable and high-efficiency $\text{Mn}_3\text{O}_4\text{-MnO}_2$ core-shell photocatalyst would be an environment-friendly material with a bright application future in water treatment field.

3.4. Possible photocatalytic mechanism

Surface area of a nanomaterial is closely related to the number of adsorption sites as well as catalytic activities, which is an indispens-

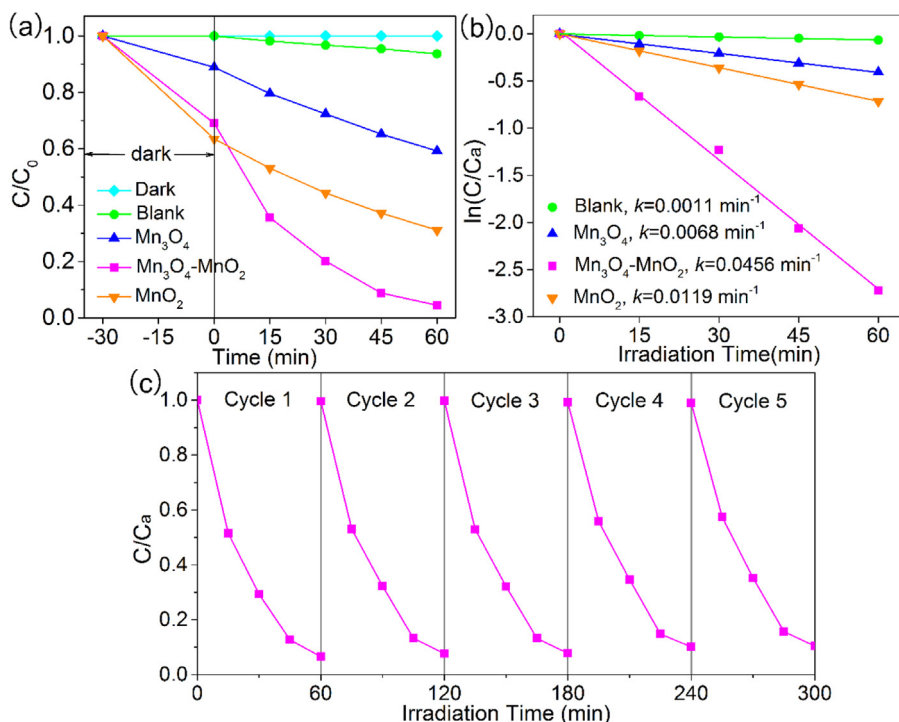


Fig. 6. (a) Photodegradation of MB by Mn_3O_4 , $\text{Mn}_3\text{O}_4\text{-MnO}_2$ and MnO_2 and blank experiment; (b) Linear fit of experimental data by first-order kinetic model; (The C_a represents the MB concentration after stirring for 30 min in dark.) (c) Consecutive cycles of $\text{Mn}_3\text{O}_4\text{-MnO}_2$ for MB degradation.

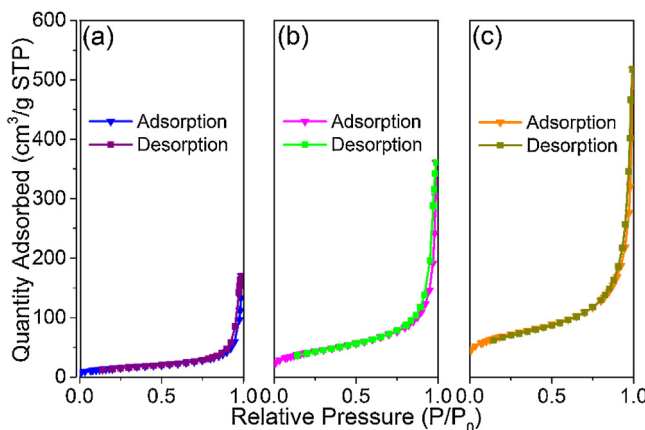


Fig. 7. N_2 adsorption-desorption isotherms of (a) Mn_3O_4 and (b) $\text{Mn}_3\text{O}_4\text{-MnO}_2$ and (c) MnO_2 .

able factor in photocatalysis [22]. The Brunauer-Emmett-Teller (BET) surface area of Mn_3O_4 , $\text{Mn}_3\text{O}_4\text{-MnO}_2$ and MnO_2 photocatalysts were measured by nitrogen (N_2) adsorption-desorption method at 77 K. The N_2 adsorption-desorption isotherms of the three samples were shown in Fig. 7. The adsorption isotherms belonged to type-IV classification [22]. The specific surface area (SSA) of Mn_3O_4 , $\text{Mn}_3\text{O}_4\text{-MnO}_2$ and MnO_2 were calculated to be 51.8, 148.3 and $171.2 \text{ m}^2/\text{g}$, respectively. The SSA of $\text{Mn}_3\text{O}_4\text{-MnO}_2$ core-shell nanosheets was significantly enhanced by doping MnO_2 , which was almost three times higher than that of pure Mn_3O_4 . The $\text{Mn}_3\text{O}_4\text{-MnO}_2$ with higher surface area could provide more activity sites, facilitating the photocatalytic process. The higher adsorption efficiency and degradation rate of $\text{Mn}_3\text{O}_4\text{-MnO}_2$ in Fig. 6(a) could partially attribute to its large surface area and more activity sites.

In order to analyze the light absorption property of Mn_3O_4 , $\text{Mn}_3\text{O}_4\text{-MnO}_2$ and MnO_2 photocatalysts, the ultraviolet-visible (UV-vis) diffuse reflectance spectra were measured and shown in Fig. 8A. The absorbance intensity of Mn_3O_4 declined sharply when light wavelength was longer than 550 nm, corresponding to a band gap of 2.2 eV [22,24]. As can be seen from Fig. 8A(c), pure MnO_2 showed a strong absorption in the ultraviolet and visible region, which was also observed in previous literature [25]. The $\text{Mn}_3\text{O}_4\text{-MnO}_2$ core-shell composite (Fig. 8A (b)) also had a strong absorption in the ultraviolet region as well as visible region. Clearly, it was MnO_2 that significantly expanded the light absorption range of $\text{Mn}_3\text{O}_4\text{-MnO}_2$ composite, which was more photo-responsive than pure Mn_3O_4 .

In order to further analyze the photocatalytic mechanism, the band structures of the pure Mn_3O_4 and MnO_2 were investigated. Firstly, the band gaps of the Mn_3O_4 and MnO_2 were acquired by employing the equation [15,16,22] below:

$$\alpha h\nu = A(h\nu - E_g)^{\frac{n}{2}} \quad (8)$$

In the equation, α , h and ν are absorption coefficient, Planck's constant and light frequency, respectively. E_g represents the band gap of a semiconductor and A is a proportionality constant. The values of n were 1 and 4 for direct transition semiconductors and indirect transition semiconductors, respectively. The value of n was 1 in this study as Mn_3O_4 and MnO_2 were both direct transition semiconductors [22,27]. Then the Eq. (8) could be expressed as Eq. (9) and the band gap (E_g) of the Mn_3O_4 and MnO_2 could be obtained by linear extrapolation. The plots of $(\alpha h\nu)^2$ versus phone energy ($h\nu$) for the pure Mn_3O_4 and MnO_2 were presented in Fig. 8B. It could be obtained that the band gaps of Mn_3O_4 and MnO_2 were 2.16 and 1.77 eV, respectively.

$$(\alpha h\nu)^2 = A^2 (h\nu - E_g) \quad (9)$$

Table 1
Calculation of the band structure of the Mn_3O_4 and MnO_2 .

Sample	E_g (eV)	χ	E_{CB} (eV)	E_{VB} (eV)
Mn_3O_4	2.16	5.57	-0.01	2.15
MnO_2	1.77	5.96	0.57	2.34

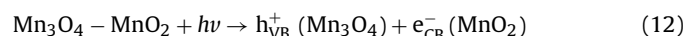
Secondly, the conduction band and valence band edges of the Mn_3O_4 and MnO_2 were estimated by the equations [22,38] below:

$$E_{CB} = \chi - E_e - \frac{1}{2}E_g \quad (10)$$

$$E_{VB} = E_{CB} + E_g \quad (11)$$

In the equations, E_{CB} and E_{VB} represent the conduction band edge and valence band edge, respectively. χ is the absolute electronegativity of a semiconductor determined by the geometric average of constituent atoms. E_e is the free energy of electrons of the semiconductor on the hydrogen scale (about 4.5 eV). The band edge values of Mn_3O_4 and MnO_2 were summarized in Table 1. The conduction band and valence band edge values of Mn_3O_4 were calculated to be -0.01 and 2.15 eV while the corresponding values of MnO_2 were 0.57 and 2.34 eV, respectively.

Accordingly, the possible photocatalytic mechanism for the high-efficiency $\text{Mn}_3\text{O}_4\text{-MnO}_2$ core-shell composite was proposed and diagrammatized in Fig. 9. Interestingly, the band structure of Mn_3O_4 and MnO_2 showed a matching band position, forming a type-II heterojunction. The formation of type-II heterojunctions is considered as an effective means for photo-carriers separation, which can improve photocatalytic performance [19]. In this study, the photocatalytic property of $\text{Mn}_3\text{O}_4\text{-MnO}_2$ core-shell composite could be significantly enhanced by the separated electron-hole pairs. In addition, the core-shell structure of composite photocatalyst was also conducive to the enhancement of photocatalytic activity [15,28]. As displayed in Fig. 9, the conduction band (-0.01 eV) and valence band (2.15 eV) of Mn_3O_4 were more negative than the conduction band (0.57 eV) and valence band (2.34 eV) of MnO_2 , which was thermodynamically beneficial for the transfer of photo-generated charge carriers [19,22]. Under visible light irradiation, the electrons (e^-) of Mn_3O_4 were excited from valence band to conduction band, leaving holes (h^+) in the valence band. Then the photo-induced electrons would transfer from the conduction band of Mn_3O_4 to that of MnO_2 . Thus, the photo-induced electrons would be enriched on MnO_2 and the holes were reserved on Mn_3O_4 , which effectively separated the photo-induced electrons and holes in space and prolonged the lifetime of carriers (Eq. (12)). Both the photo-induced holes and electrons were the dominant active centers for the visible light catalysis. The holes could react with hydroxyl ions, forming hydroxyl radicals in the valence band of Mn_3O_4 (Eq. (13)). Meanwhile, the superoxide radical anions could be generated in the conduction band of MnO_2 by interactions between the electrons and dissolved oxygen (Eq. (14)).



To further prove the efficient separation of photo-carriers in $\text{Mn}_3\text{O}_4\text{-MnO}_2$ composite photocatalyst, the transient photocurrent response and electrochemical impedance spectroscopy (EIS) of the samples were measured. As shown in Fig. 10A, the photocurrent of the three photocatalysts were stable under visible light, and the photocurrent sharply decreased as the lamp was turned off. Noticeably, the photocurrent of $\text{Mn}_3\text{O}_4\text{-MnO}_2$ was much higher than that of pure Mn_3O_4 and MnO_2 , indicating the effective separation and prolonged lifetime of charge carriers in $\text{Mn}_3\text{O}_4\text{-MnO}_2$ composite [15,39]. Besides, the charge transfer resistance at the

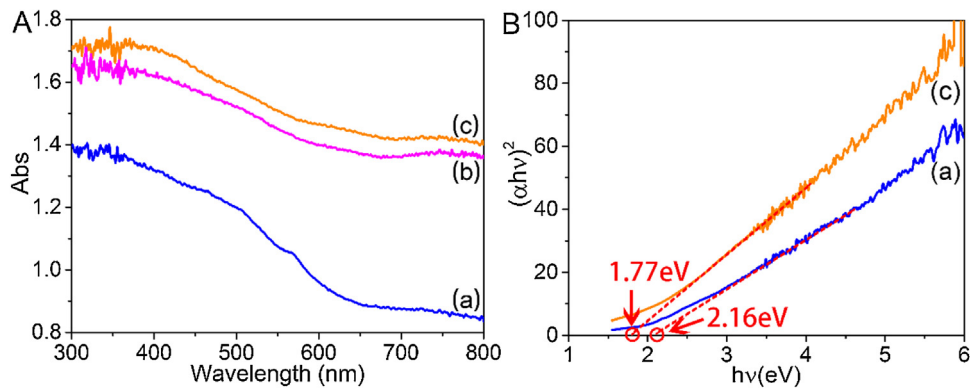


Fig. 8. (A) UV-vis diffuse reflectance spectra of (a) Mn₃O₄, (b) Mn₃O₄-MnO₂ and (c) MnO₂; (B) Plots of $(\alpha h\nu)^2$ versus phone energy ($h\nu$) of (a) Mn₃O₄ and (c) MnO₂.

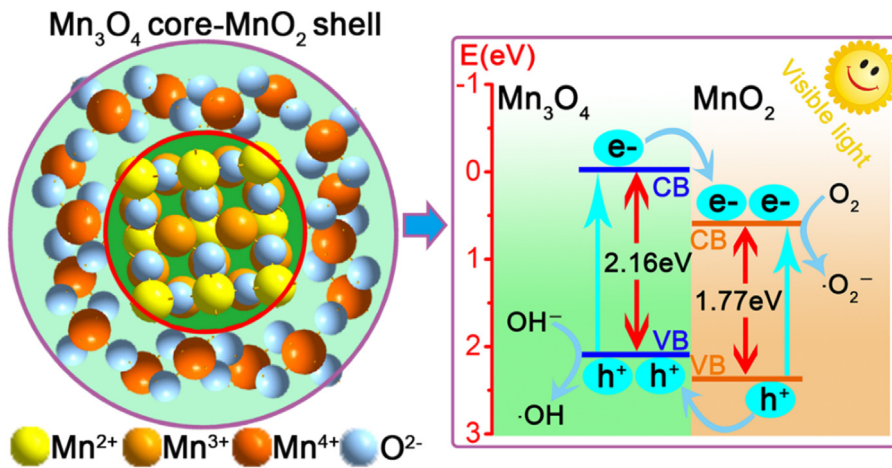


Fig. 9. Schematic interpretation of the photocatalytic mechanism for the high-efficiency Mn₃O₄-MnO₂ core-shell composite.

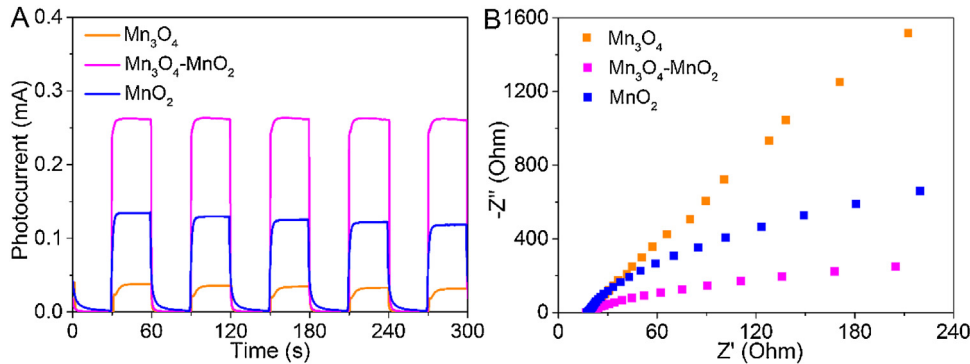


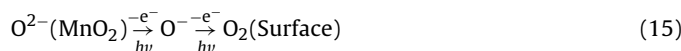
Fig. 10. (A) Transient photocurrent response of Mn₃O₄, Mn₃O₄-MnO₂ and MnO₂ under visible light irradiation with light on/off cycles; (B) Electrochemical impedance spectroscopy of Mn₃O₄, Mn₃O₄-MnO₂ and MnO₂ under visible light irradiation.

electrode/electrolyte interface was also analyzed. As is well known, a smaller diameter indicates a lower charge transfer resistance (i.e. more facile charge transfer) in Nyquist plots [15,39]. As shown in Fig. 10B, the Mn₃O₄-MnO₂ composite presented the smallest diameter among the three samples, indicating the lowest interfacial charge-transfer resistance. The higher charge separation and transfer efficiency of Mn₃O₄-MnO₂ composite enhanced the photocatalytic activity.

Moreover, the radical-trapping experiment showed that the superoxide radicals played the most vital role in the photo-degradation process, followed by the holes and hydroxyl radicals. Benzoquinone (BQ), disodium ethylenediamine tetraac-

etate (Na₂EDTA) and *tert*-butyl alcohol (TBA) were employed as the probes of superoxide radicals, holes and hydroxyl radicals respectively [22] to identify the role of each active specie in the degradation process. As shown in Fig. S6, the removal efficiency of MB decreased from 93.5% to 47.0%, 61.3% and 69.1% respectively after adding the three scavengers to MB solution. Results indicated that superoxide radicals, holes and hydroxyl radicals were all played active parts in MB degradation, while the role of superoxide radicals was the most significant. Besides, the surface oxygen of Mn₃O₄-MnO₂ composite also made contributions to the formation of excited-state oxygen species during photocatalytic oxidation. The removal rate of MB with Mn₃O₄-MnO₂ photocatalyst decreased

by 34.2% in nitrogen atmosphere (supplied in Fig. S8A). The MB solution showed a definite degradation in the first 15 min under visible light irradiation, then the degradation rate became very slow. This was because the absorbed oxygen and bulk oxygen of amorphous MnO₂ in turn formed active oxygen species with electrons at the early stage (Eqs. (14)–(15)) [32,40]. However, the movement of lattice oxygen from Mn₃O₄–MnO₂ to the surface normally needed thermal energy to overcome the large lattice energy, which could not form the active oxygen at room temperature in general [32]. The amount of active oxygen species dropped sharply in oxygen free conditions. Therefore, the degradation rate dramatically declined in the absence of atmospheric oxygen (Fig. S8A). Interestingly, the Mn₃O₄–MnO₂ core-shell composite still possessed high catalytic activity after five cycles in Fig. 6(c). Although the surface oxygen and the bulk oxygen were evolved, the oxygen vacancies on Mn₃O₄–MnO₂ surface would be replenished by dissolved oxygen in water (Eq. (16)) [32], which was further demonstrated in Fig. S8B in Supporting information. It can be inferred that the composite photocatalyst had strong self-regeneration capacity in air to maintain the outstanding catalytic performance.



4. Conclusion

In summary, a novel Mn₃O₄–MnO₂ valence state heterojunction was fabricated by a facile and energy-effective hydrothermal method at 363 K. The XPS, XRD, SEM and TEM were used for characterization. Results showed that the Mn₃O₄–MnO₂ nanosheets with core-shell structure was composed of crystalline Mn₃O₄ (tetragonal hausmannite) and amorphous α-MnO₂. In addition, the formation mechanism of the photocatalysts were discussed based on their composition and chemical stoichiometry. The specific surface area and visible light absorption of Mn₃O₄–MnO₂ composite were significantly enhanced by doping MnO₂ compared to the pure Mn₃O₄. The Mn₃O₄–MnO₂ composite possessed the best photocatalytic activity with the removal efficiency of MB reaching 93.5% in 1 h under visible light irradiation. Further exploration of the mechanism indicated that the formation of the type II heterojunction in Mn₃O₄–MnO₂ composite might achieve the spatial separation of photo-induced carriers effectively. Moreover, the superoxide radicals played an important role in photo-degradation process, followed by the holes and hydroxyl radicals. The surface oxygen of Mn₃O₄–MnO₂ was also took part in the formation of active oxygen species. Besides, the Mn₃O₄–MnO₂ photocatalyst exhibited self-regeneration ability with atmospheric oxygen. These findings would provide a new perspective for manganese oxides applied in photocatalysis field.

Acknowledgements

This work was supported by the National Science and Technology Major Project of Twelfth Five Years (Nos.2014ZX07201-012-2 and 2013ZX07201007-002), the National Natural Science Foundation of China (No. 51208140) and the Frontier and Application Basis Research Project of Chongqing (No. cstc2015jcyjA1050).

Appendix A. Supplementary data

Supplementary data associated with this article can be found, in the online version, at <http://dx.doi.org/10.1016/j.apcatb.2016.09.065>.

References

- [1] Y. Luo, W. Guo, H.H. Ngo, L.D. Nghiem, F.I. Hai, J. Zhang, S. Liang, X.C. Wang, *Sci. Total Environ.* 473 (2014) 619–641.
- [2] T. Ito, Y. Adachi, Y. Yamanashi, Y. Shimada, *Water Res.* 100 (2016) 458–465.
- [3] Y. Ren, L. Lin, J. Ma, J. Yang, J. Feng, Z. Fan, *Appl. Catal. B: Environ.* 165 (2015) 572–578.
- [4] A. Alsbiae, B.J. Smith, L. Xiao, Y. Ling, D.E. Helbling, W.R. Dichtel, *Nature* 529 (2015) 190–194.
- [5] Z. Hasan, S.H. Jhung, J. Hazard. Mater. 283 (2015) 329–339.
- [6] Z. Xing, W. Zhou, F. Du, L. Zhang, Z. Li, H. Zhang, W. Li, *ACS Appl. Mater. Interfaces* 6 (2014) 16653–16660.
- [7] B. Patterson, M. Shackleton, A. Furness, J. Pearce, C. Descourvieres, K. Linge, F. Busetti, T. Spadek, *Water Res.* 44 (2010) 1471–1481.
- [8] S. Hussain, J. van Leeuwen, C. Chow, S. Beecham, M. Kamruzzaman, D. Wang, M. Drikas, R. Aryal, *Chem. Eng. J.* 225 (2013) 394–405.
- [9] B. Wols, C. Hofman-Caris, *Water Res.* 46 (2012) 2815–2827.
- [10] D. Spasiano, R. Marotta, S. Malato, P. Fernandez-Ibanez, I. Di Somma, *Appl. Catal. B: Environ.* 170 (2015) 90–123.
- [11] M.N. Chong, B. Jin, C.W.K. Chow, C. Saint, *Water Res.* 44 (2010) 2997–3027.
- [12] Z. Xing, Z. Li, X. Wu, G. Wang, W. Zhou, *Int. J. Hydrogen Energy* 41 (2016) 1535–1541.
- [13] H. Lee, J. Choi, S. Lee, S.-T. Yun, C. Lee, J. Lee, *Appl. Catal. B: Environ.* 138 (2013) 311–317.
- [14] L. Zhang, Z. Xing, H. Zhang, Z. Li, X. Wu, X. Zhang, Y. Zhang, *Appl. Catal. B: Environ.* 180 (2016) 521–529.
- [15] L. Liu, Y. Qi, J. Lu, S. Lin, W. An, Y. Liang, W. Cui, *Appl. Catal. B: Environ.* 183 (2016) 133–141.
- [16] O.F. Lopes, K.T. Carvalho, A.E. Nogueira, W. Avansi, C. Ribeiro, *Appl. Catal. B: Environ.* 188 (2016) 87–97.
- [17] X. Liu, Z. Xing, H. Zhang, W. Wang, Y. Zhang, Z. Li, X. Wu, X. Yu, W. Zhou, *ChemSusChem* 9 (2016) 1118–1124.
- [18] H. Wang, L. Zhang, Z. Chen, J. Hu, S. Li, Z. Wang, J. Liu, X. Wang, *Chem. Soc. Rev.* 43 (2014) 5234–5244.
- [19] Y. Wang, Q. Wang, X. Zhan, F. Wang, M. Safdar, J. He, *Nanoscale* 5 (2013) 8326–8339.
- [20] G. Wang, B. Huang, L. Wang, Z. Wang, Z. Lou, X. Qin, X. Zhang, Y. Dai, *Chem. Commun.* 50 (2014) 3814–3816.
- [21] B. Jiang, X. Peng, Y. Qu, H. Wang, C. Tian, Q. Pan, M. Li, W. Zhou, H. Fu, *ChemCatChem* 6 (2014) 2553–2559.
- [22] G. Wang, B. Huang, Z. Lou, Z. Wang, X. Qin, X. Zhang, Y. Dai, *Appl. Catal. B: Environ.* 180 (2016) 6–12.
- [23] K.A.M. Ahmed, H. Peng, K. Wu, K. Huang, *Chem. Eng. J.* 172 (2011) 531–539.
- [24] Y. Wu, D. Chu, P. Yang, Y. Du, C. Lu, *Catal. Sci. Technol.* 5 (2015) 3375–3382.
- [25] M. Xue, L. Huang, J.-Q. Wang, Y. Wang, L. Gao, J.-h. Zhu, Z.-G. Zou, *Nanotechnology* 19 (2008) 185604.
- [26] S. Liu, H. Liu, G. Jin, H. Yuan, *RSC Adv.* 5 (2015) 45646–45653.
- [27] B. Nanda, A.C. Pradhan, K. Parida, *Microporous Mesoporous Mater.* 226 (2016) 229–242.
- [28] Z. Zhao, J. Liu, F. Cui, H. Feng, L. Zhang, *J. Mater. Chem.* 22 (2012) 9052–9057.
- [29] C. Wei, C. Xu, B. Li, H. Du, D. Nan, F. Kang, *J. Power Sources* 234 (2013) 1–7.
- [30] Z.-Y. Tian, P. Mountapbeme Kouotou, N. Bahlawane, P.H. Tchoua Ngamou, *J. Phys. Chem. C* 117 (2013) 6218–6224.
- [31] J. Liu, X. Ge, X. Ye, G. Wang, H. Zhang, H. Zhou, Y. Zhang, H. Zhao, *J. Mater. Chem. A* 4 (2016) 1970–1979.
- [32] H. Cao, S.L. Suib, *J. Am. Chem. Soc.* 116 (1994) 5334–5342.
- [33] A. Yuan, Q. Zhang, *Electrochim. Commun.* 8 (2006) 1173–1178.
- [34] Y. Sun, Y. Yin, B.T. Mayers, T. Herricks, Y. Xia, *Chem. Mater.* 14 (2002) 4736–4745.
- [35] F. Koroleff, *Acta Chem. Scand.* 1 (1947) 503–506.
- [36] A. Giri, N. Goswami, M. Pal, M.T.Z. Myint, S. Al-Harthi, A. Singha, B. Ghosh, J. Dutta, S.K. Pal, *J. Mater. Chem. C* 1 (2013) 1885–1895.
- [37] S.A.B. Asif, S.B. Khan, A.M. Asiri, *Nanoscale Res. Lett.* 10 (2015) 1–10.
- [38] C. Tang, E. Liu, J. Wan, X. Hu, J. Fan, *Appl. Catal. B: Environ.* 181 (2016) 707–715.
- [39] J. Di, J. Xia, M. Ji, B. Wang, Y. Sheng, Z. Qi, Z. Chen, H. Li, *Appl. Catal. B: Environ.* 183 (2015) 254–262.
- [40] J.C. Lin, J. Chen, S.L. Suib, M.B. Cutlip, J.D. Freihaut, *J. Catal.* 161 (1996) 659–666.